

Chapter 18

AIE Luminogens for Three-Photon Fluorescence Bioimaging



Dan Wang and Jun Qian

Abstract Aggregation-induced emission luminogens (AIEgens) have received intense scientific attention for biomedical applications from molecular sensing through cellular imaging to cancer diagnosis. Compared with conventional one-photon or two-photon fluorescence imaging technologies, three-photon fluorescence microscopy (3PFM) is more powerful with higher resolution and deeper tissue penetration. 3PFM can dramatically reduce the out-of-focus fluorescence in regions out of the focal plane, and allow a wide variety of existing AIEgens to be excited at the 1000–1700 nm region with less photon attenuation caused by tissue scattering. In this chapter, a brief introduction on the concepts of AIEgens and 3PFM was given, followed by presenting a focused overview on their current applications for fluorescence imaging in cells, zebrafish embryos, and mice. Some insights on the challenges and opportunities in this important field were also discussed.

18.1 Introduction

Fluorescence imaging is among the most widely used techniques in biomedical research to visualize morphological details for bio-species, ranging from living cells to animals [1–3]. To use fluorescence for bioimaging, one can use endogenous fluorescence (autofluorescence) or one may label the biological specimen (a biomolecule, an organelle, a cell, or a tissue) with a suitable fluorescent probe whose distribution will become distinct under light excitation [4]. A number of endogenous

D. Wang

State Key Laboratory of Organic-Inorganic Composites, College of Chemical Engineering,
Beijing University of Chemical Technology, Beijing, China

J. Qian (✉)

State Key Laboratory of Modern Optical Instrumentations, Centre for Optical and
Electromagnetic Research, College of Optical Science and Engineering, Zhejiang University,
Hangzhou, China
e-mail: qianjun@zju.edu.cn

fluorophores, such as flavins, lipofuscin, and nicotinamide adenine dinucleotide, have been used for monitoring cellular processes [5–7]. Some of them also exhibit sufficiently strong two-photon excited emission, making them useful for cellular imaging [6, 7]. However, there are many biological specimens and processes that are not able to be imaged or probed by using intrinsic fluorescence due to the lack of endogenous fluorophores. In these cases, exogenous fluorophores is needed to label these biological specimens for bioimaging with high signal-to-noise ratio (SNR) [8–10].

Organic dyes with high fluorescence quantum yields have been the most commonly used exogenous fluorophores for bioimaging in the past century [11]. The development of nanotechnology in the last decades has opened up new frontiers in organic dyes by encapsulating or doping them into nanoparticles for various applications [12–14]. The tailor-made nanoprobes based on organic dyes are desirable for bioimaging with (1) dispersability (solubility) of the fluorophore in the biological medium to be probed, (2) specific association with a target molecule, organelle, or cell, and (3) environmental stability [15–17]. However, the majority of common fluorophores such as fluoresceins, rhodamines, and cyanines suffer from aggregation caused quenching (ACQ) effect due to the π - π stacking [18, 19]. Therefore, these organic dyes are usually loaded with very low concentrations in nanoparticles, which are easily photobleached during long-term light irradiation [20]. The concept of aggregation-induced emission was pioneered by Tang and coworkers in 2001, when the 1-methyl-1,2,3,4,5-pentaphenylsilole molecules are found to be non-emissive dissolving in benign solvent but highly luminescent in the aggregation states [21, 22]. To date, a variety of AIE luminogens (AIEgens) with emission from blue through red to near-infrared region have been developed, including but not limited to tetraphenylethene (TPE) [23], tetraphenylsilole (TPS) [24], and distyrylanthracene (DSA) derivatives [25]. Contrary to conventional organic dyes, the AIE molecules can be encapsulated or doped in nanoparticles with high concentrations to form “bright” nanoprobes regardless of the ACQ problem and have been proven as excellent exogenous fluorophores for bioimaging in both cells and animals [26].

Another problem for fluorescence bioimaging is that most AIEgens are excited by one-photon absorption in the short-wavelength spectral region between 350 and 600 nm [27]. At these wavelengths, the significant Rayleigh scattering and autofluorescence of biological tissues such as fur, skin, and food in the subject studied, limit the depth access [28]. Some of these problems have been overcome with the use of multiphoton microscopy techniques [29]. In multiphoton microscopy, the AIEgens are excited by multiphoton absorption referring to a nonlinear optical absorption process in which more than one photon are absorbed simultaneously by a single molecule to reach a real excited state [30–32]. Typically, the well-developed two-photon microscopy can use a short-pulsed (e.g., femtoseconds, abbreviated as fs) laser with output wavelength in the traditional near-infrared region (NIR-I, 700–950 nm) as the excitation source and produce fluorescence in the visible range, enabling scientists to visualize *in vivo* and *ex vivo* tissue morphology and physiology at a cellular level deep within scattering tissue [33–35]. Furthermore, in recent years, three-photon bioimaging based on the excitation of light in the second near-infrared

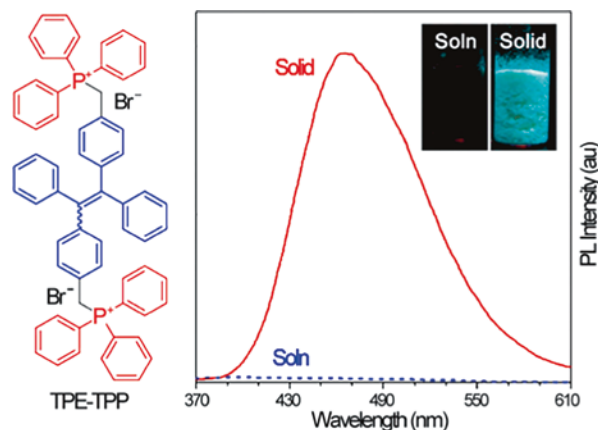
window (NIR-II, 1000–1700 nm) has proven more desirable than visible (450–750 nm) and traditional NIR-I imaging (750–900 nm) owing to reduced photon scattering, deeper tissue penetration, and lower autofluorescence [36]. Three-photon fluorescence microscopy (3PFM) dramatically reduces the out-of-focus background in regions far from the focal plane, improving the SNR by orders of magnitude when compared to 2PFM [36]. In addition, three-photon excitation (3PE) allows a wide variety of existing AIEgens to be excited at the NIR-II spectral window (equivalent to a one-photon excitation of 330–560 nm), eliminating the practical difficulty caused by the lack of AIEgens at the NIR-II spectral region for 2PFM [33, 37].

In light of the tremendous progress that has been achieved in this field, it is necessary to summarize the recent research results concerning AIEgens for three-photon fluorescence bioimaging. Herein, a brief introduction on the applications of AIEgens for three-photon fluorescence bioimaging of cells, zebrafish embryos, and mice is given. Significant advances achieved by our and other groups in the past few years are summarized. Some challenges and opportunities for the use of AIEgens in biomedical diagnosis and therapy will be put forward, based on our own understanding of this field.

18.2 AIEgens for Three-Photon Fluorescence Imaging in Cells

The tetraphenylethene-triphenylphosphonium (TPE-TPP) is a typical AIE molecule with cyan emission as shown in Fig. 18.1 [38]. The *N,N*-Dimethylformamide (DMF) solution of TPE-TPP was almost non-emissive, while the solid state is highly luminescent [38, 39]. TPE-TPP has proven to be a well-suited imaging agent for mitochondrial targeting and morphological change tracking, due to its high specificity to mitochondria, superior photostability, and appreciable tolerance to microenvironment change [38, 40]. However, the TPE-TPP exhibits short-wavelength fluorescence

Fig. 18.1 Chemical structure of TPE-TPP; fluorescence spectra of TPE-TPP in solid and solution (soln) states. Inset: Photographs of DMF solution (left) and solid powder (right) of TPE-TPP taken under UV irradiation. Concentration of TPE-TPP: 10 μ M; excitation wavelength: 321 nm. Adapted with permission from [38]. Copyright (2013) American Chemical Society



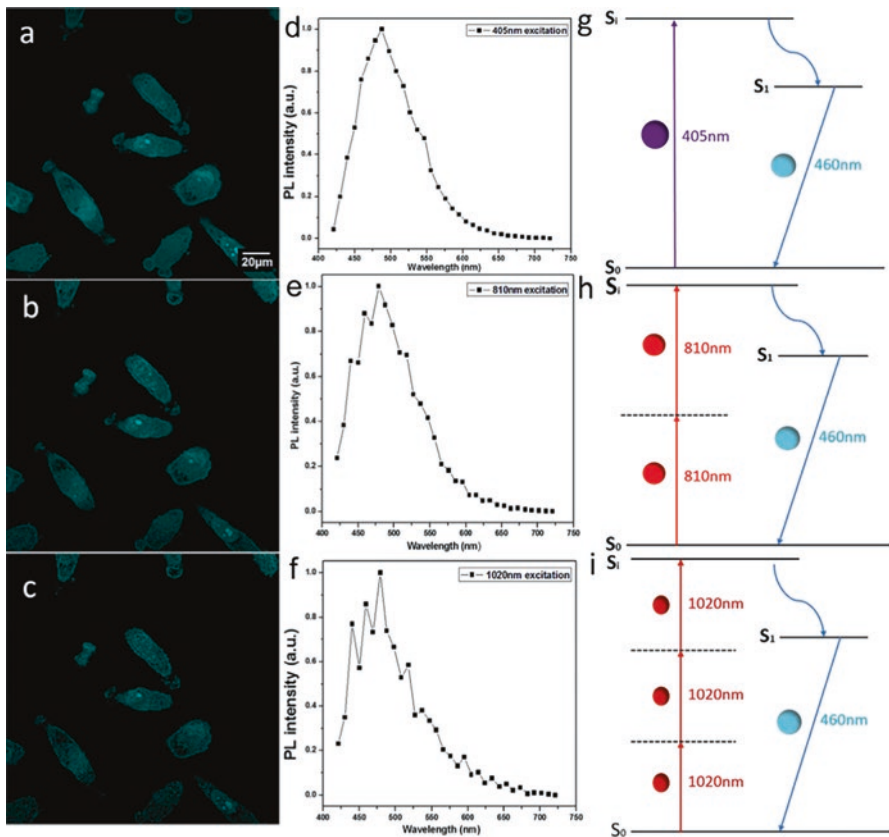


Fig. 18.2 (a–c) One-, two-, and three-photon microscopic images of TPE-TPP treated HeLa cells, with an excitation of (a) 405 nm-CW, (b) 810 nm-fs, and (c) 1020 nm-fs lasers. (d) One-, (e) two- and (f) three-photon fluorescence spectra of TPE-TPP labeled cells. (g–i) Diagrams showing the proposed mechanism for one-, two-, and three-photon excitation and luminescence. S_i is the higher (electronic or vibronic) state; S_1 is the lower radiative state; S_0 is the ground state. Under our experimental conditions, luminescence occurred as a result of radiative transitioning between S_1 and S_0 . Adapted with permission from [40]. Copyright (2015) Nature Publishing Group

emission (centered at 466 nm) and should be excited by ultraviolet (UV) light for one-photon fluorescence bioimaging [38–40].

Figure 18.2a shows one-photon confocal microscopic imaging of HeLa cells labeled with TPE-TPP using 405 nm CW laser excitation by Zhu et al. [40]. The fluorescence signal of TPE-TPP along with its spectrum was clearly determined from the HeLa cells, demonstrating the effective uptake of TPE-TPP by cells. Two- and three-photon fluorescence images of TPE-TPP in HeLa cells were obtained by using 810 nm fs laser and 1020 nm fs laser as the excitation light. Figure 18.2b, c show the two- and three-photon fluorescence signals of TPE-TPP in HeLa cells. The fluorescence spectra of TPE-TPP in HeLa cells from one-, two-, and three-photon excitation exhibit similar trends in the range of 425–600 nm with a maximum peak

at 470 nm (Fig. 18.2d–f). These spectra agreed well with the fluorescence spectra of TPE-TPP measured in the solid state (Fig. 18.1), suggesting that the excitons in the TPE-TPP eventually relaxed to the same state for all the excited fluorescence processes (Fig. 18.2g–i). As illustrated in Fig. 18.2h, the energy of one 810 nm photon is lower than the bandgap between the ground state (S_0) and excited state (S_1) of TPE-TPP. The emission of TPE-TPP by 810 nm fs laser irradiation should be generated by simultaneous absorption/excitation of two photons [40]. In like manner, the sum energy of two 1020 nm photons is not high enough to excite the TPE-TPP from S_0 to S_1 . Therefore, the observed emission of TPE-TPP by 1020 nm fs irradiation is caused by the simultaneous absorption of three photons (Fig. 18.2i). Zhu et al. also determined the three-photon absorption cross-section of TPE-TPP molecules at 1020 nm, which was $2.54 \times 10^{-80} \text{ cm}^6 \text{ s}^2$.

The advantage of higher SNR of three-photon fluorescence bioimaging of TPE-TPP in cells than those of one and two-photon fluorescence imaging was also demonstrated. The intrinsic endogenous fluorophores in cells usually generate autofluorescence in the region of 400–550 nm [41]. TPE-TPP emits cyan light with an emission peak at 470 nm (Fig. 18.1) [38], which is hardly distinguished from the cellular autofluorescence during one-photon excited cell imaging [40]. Carbonyl cyanide m-chlorophenylhydrazone (CCCP) is a commonly used chemical protonophore that directly interferes with mitochondrial function and induces apoptosis by changing the mitochondria membrane potential ($\Delta\Psi_m$) of cells [40, 42]. By adding different quantities of CCCP in the cells to tune the $\Delta\Psi_m$, Zhu et al. obtained HeLa cells with different uptake efficiency of TPE-TPP and compared the SNR data of one-, two-, and three-photon fluorescence imaging under the excitation of a 405 nm continuous wave (CW) laser, a 810 nm fs laser, and a 1020 nm fs laser. The one-, two-, and three-photon fluorescence intensity from TPE-TPP stained cells became gradually weaker when increasing the dosage of CCCP (Fig. 18.3), demonstrating that a decreasing concentration gradient formed due to the increasing of CCCP.

The changes of fluorescence intensity from cells treated with various dosages of CCCP are present in Fig. 18.4. Due to the inhibiting effect of 8 μL CCCP in the experiments, the fluorescence intensity observed from cells reduced by half under one-photon (405 nm) excitation. However, the fluorescence intensities have declined more than 75% and 90% under two-photon (810 nm) and three-photon (1020 nm) excitation, respectively (Fig. 18.4). As discussed above, the observed fluorescence signal from cells was composed of the emission from TPE-TPP and the endogenous fluorophores. As for the fluorescence images obtained from cells treated with 8 μL CCCP under 405 nm CW excitation, the fluorescence signal was most likely auto-fluorescence of the endogenous fluorophores. However, most endogenous fluorophores in the cells have relatively small two- and three-photon absorption cross sections, and the autofluorescence was hardly detected when using 810 nm fs laser and 1020 nm fs laser as the excitation sources [40]. The TPE-TPP, which has higher three-photon absorption efficiency than the endogenous fluorophores, are easy to be detected in the cells for three-photon fluorescence imaging. These results demonstrate that multiphoton microscopy provides higher SNR of imaging, which can help us monitor tiny changes of TPE-TPP in cells without the influence of autofluorescence.

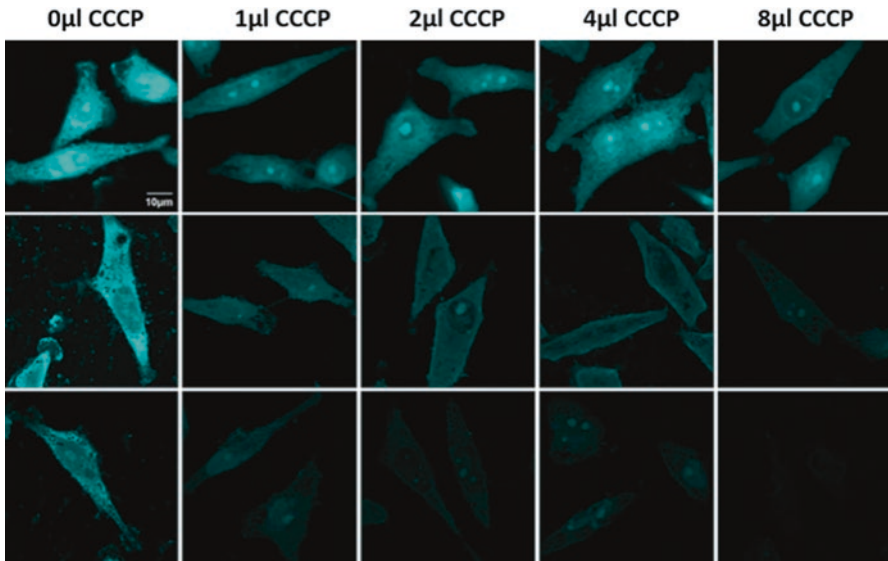


Fig. 18.3 Fluorescence imaging of TPE-TPP labeled HeLa cells (cells have been treated with different dosages of CCCP, as shown on the top of the figures) excited by 405 nm CW (top row), 810 nm fs (middle row), and 1020 nm fs (bottom row) lasers, respectively. Adapted with permission from [40]. Copyright (2015) Nature Publishing Group

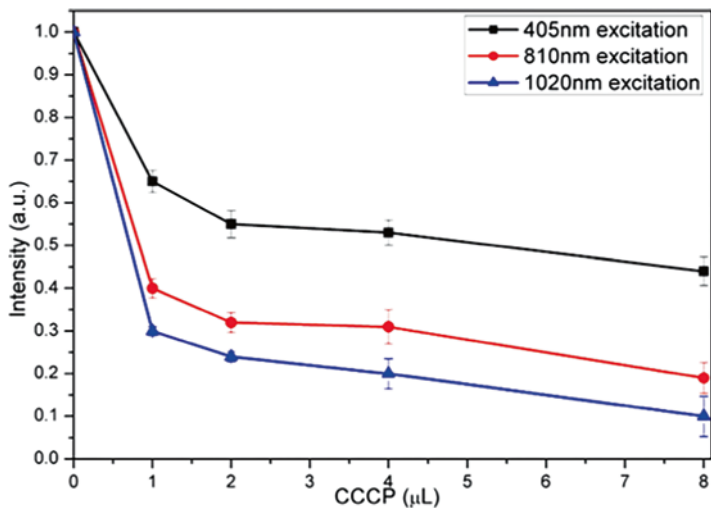


Fig. 18.4 Normalized fluorescence intensity of TPE-TPP stained cells with treatment of increasing dosages of CCCP, under one- (black curve), two- (red curve), and three-photon (blue curve) excitation. Adapted with permission from [40]. Copyright (2015) Nature Publishing Group

Compared with two-photon fluorescence bioimaging using 810 nm fs laser for excitation, the use of 1020 nm fs laser for three-photon fluorescence bioimaging also showed lower phototoxicity. Figure 18.5 shows the optical microscopic images of HeLa cells scanned by 810 nm fs laser and 1020 nm fs laser reported by Zhu et al. [40]. After irradiation by a 810 nm fs laser (15 mW after the 60 \times objective lens, the imaging area was enlarged for 2 times via the software) for 5 min, a burned spot was observed from the HeLa cells. The burned spot illustrated the potential damage of cells by the light, which was attributed to the multiphoton absorption of the cell and the intracellular destructive plasma formation under 810 nm fs laser excitation [43]. However, no significant photodamage was observed from HeLa cells under the irradiation of 1020 nm fs laser for 5 min, although a higher excitation power was applied (30 mW after the 60 \times objective lens). These results demonstrated that the fs lasers in the NIR-II spectral region with lower photon energy than those in the NIR-I spectral region generate less photodamage to cells [40].

In another work, Mandal et al. [44] report the experimental observation of aggregation-induced enhanced luminescence upon three-photon excitation in aggregates formed from a class of unsymmetrical cyanostilbene derivatives. Figure 18.6a shows the molecular structure of folic acid (FA) attached unsymmetrical cyanostilbene derivative. The hydrophilic side chains preferably formed well-dispersed spherical nanoaggregates (FA-agg) in a dimethyl sulfoxide (DMSO)/water mixture solvent. According to the TEM characterization, the FA-agg showed solid spherical nanoparticles with an average diameter of 150 nm. The FA-agg dispersed well in aqueous-organic mixture and exhibited a three-photon cross-section of $6 \times 10^{-80} \text{ cm}^6 \text{ s}^2 \text{ photon}^{-2}$. Figure 18.6c shows the photograph of the three-photon

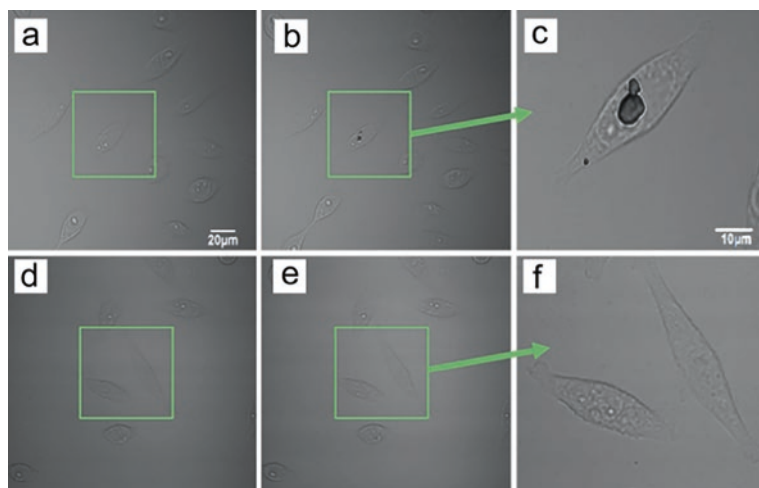


Fig. 18.5 Transmission imaging of HeLa cells (**a**, **d**) before and (**b**, **e**) after one area is scanned by the 810 nm (**b**) and 1020 nm (**e**) fs laser for ~5 min. (**c**, **f**) Magnified areas scanned by the 810 nm (**c**) and 1020 nm (**f**) fs laser. Adapted with permission from [40]. Copyright (2015) Nature Publishing Group

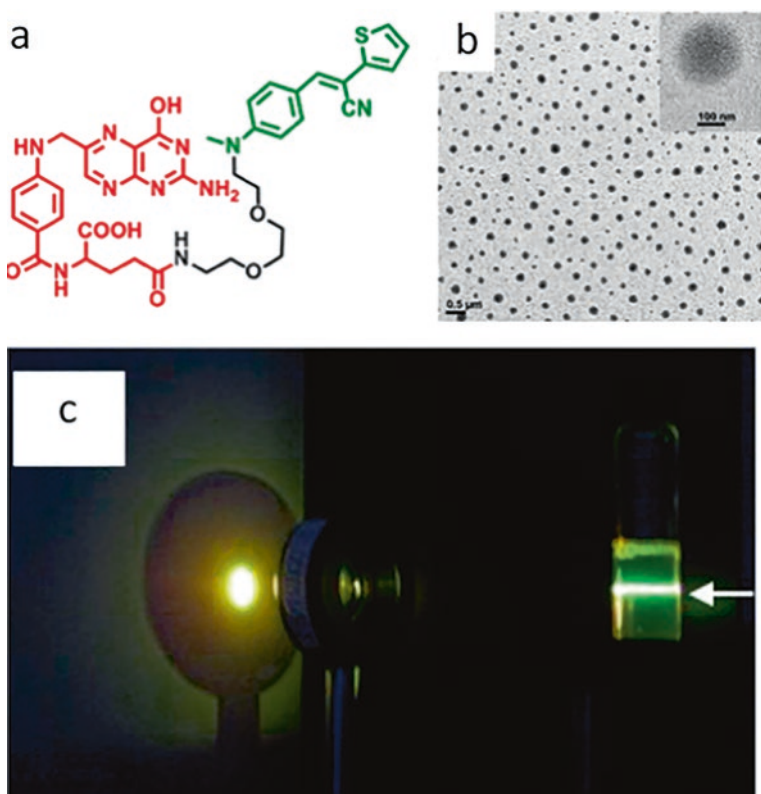


Fig. 18.6 (a) Molecular structures of folic acid attached unsymmetrical cyanostilbene derivative. (b) A typical TEM image of the nanoaggregates of FA-agg prepared by injecting the concentrated solution of corresponding compounds in DMSO (4×10^{-3} M, 50 μ L) into water (3.95 mL). The final concentration is 5×10^{-5} M, and the proportion of DMSO in water is 1.25 vol%. (c) A typical photograph showing the three-photon image from FA-agg reflected on a white screen for clarity. The white arrow indicates the direction of incident laser beam. Adapted with permission from [44]. Copyright (2015) American Chemical Society

aggregation-induced luminescence observed from FA-agg in DMSO/water mixture solution.

Three different cell lines (HEK293 healthy cell line, MCF7 cancerous cell line, and HeLa cancerous cell line) with different folate receptor expression levels were selected to demonstrate the targeted bioimaging capability of FA-agg. Among them, the HeLa cell line is well known for its high expression of the folate receptor as a positive control (FA+), whereas MCF7 and HEK293 cell lines have a low expression of the folate receptor as negative controls (FA-) [44, 45]. All of the cell lines were incubated with FA-agg in respective sets for 4 h. An aggregate concentration of 47.5 μ m was used after optimization by several trials in order to achieve uniform distribution of aggregates for bioimaging. Figure 18.7 shows the results of the three-photon bioimaging experiments upon excitation at 1300 nm and emissions collected

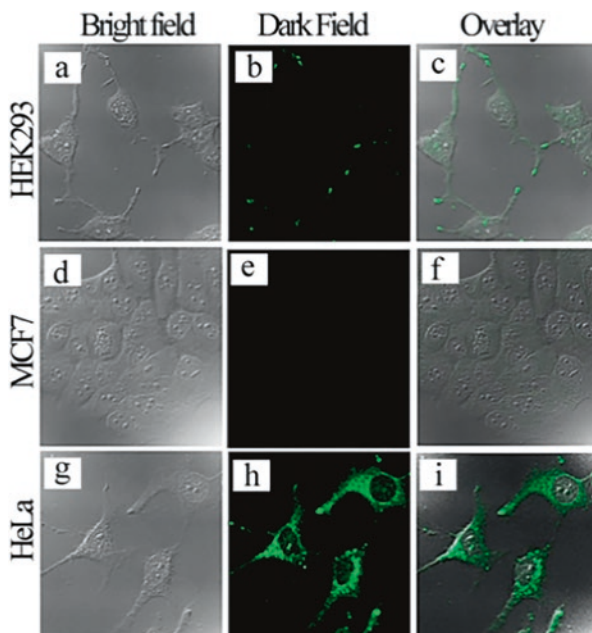


Fig. 18.7 Three-photon microscopic images of HEK293 (**a–c**), MCF7 (**d–f**), and HeLa (**g–i**) cells incubated with FA-agg for 4 h. Excitation was at 1300 nm, and emission was collected at 500–600 nm. Adapted with permission from [44]. Copyright (2015) American Chemical Society

at 500–600 nm. For HEK293 and MCF7 cells, no obvious endocytosis of FA-agg was observed. However, enhanced endocytosis of FA-agg was observed in HeLa cancer cells, which was clearly evidenced from both the dark field (Fig. 18.7h) and overlay (Fig. 18.7i) images. As compared with bioimaging results under one- and two-photon excitations (Fig. 18.8), the obtained three-photon bioimaging showed better performance. These studies present a novel paradigm of using AIEgens for high-resolution three-photon bioimaging *in vitro* [40, 44].

18.3 AIEgens for Three-Photon Fluorescence Imaging in Zebrafish

Zebrafish is an organism emerging as a model of choice to evaluate biomaterials from various aspects, such as nanotoxicity, imaging, and gene therapy [46, 47]. This organism is easy to use due to its low maintenance cost, optical transparency, and significant similarity to the human genome [48, 49]. The zebrafish body is transparent during early embryonic development and hence it is easy to observe the *in vivo* transport, ratiometric fluorescence probe, toxicity, and biocompatibility of various nanoparticles, as well as real-time drug screening at this stage [50–52].

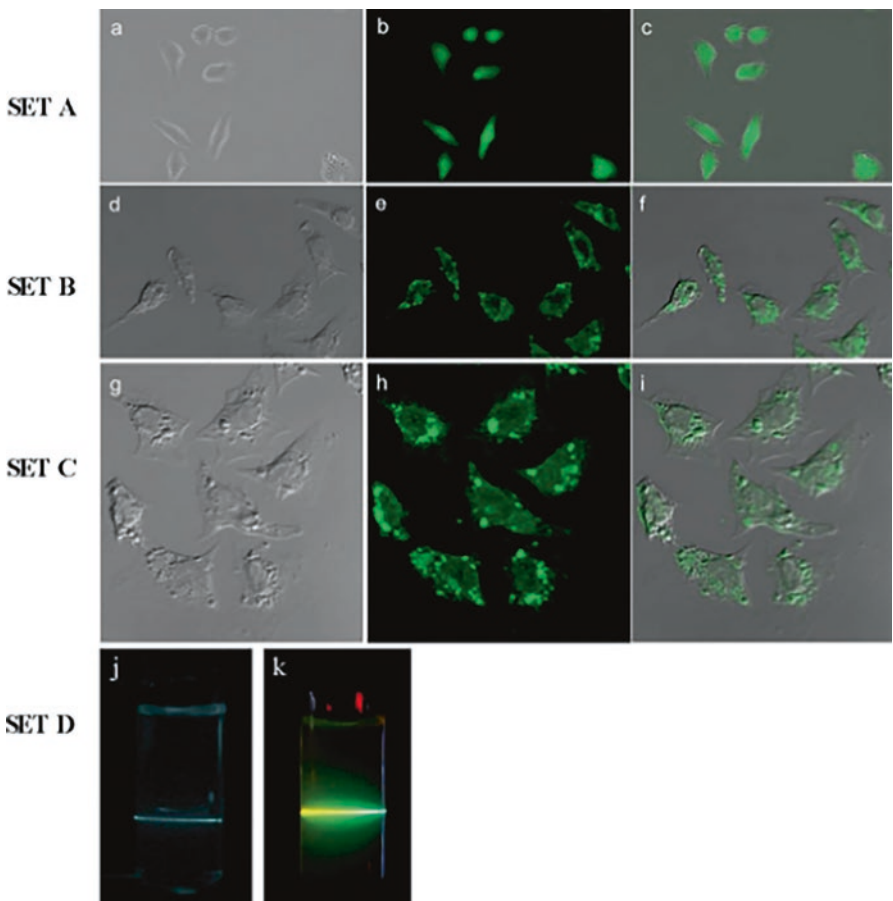


Fig. 18.8 Fluorescence bioimaging results of HeLa cells incubated with FA-agg upon excitation at (Set A, **a–c**) 405 nm (emission collected from 500 to 600 nm), (Set B, **d–f**) 850 nm (emission collected from 500 to 600 nm), and (Set C, **g–i**) 1300 nm (emission collected from 500 to 600 nm). Set D is the photographs showing (**j**) 2P (exc. 850 nm) and (**k**) 3P (exc. 1300 nm) excited fluorescence from FA-agg in PBS buffer at pH 7.4, indicating that 3P (exc. 1300 nm) excited fluorescence is stronger than 2P (exc. 850 nm) excited fluorescence. Adapted with permission from [44]. Copyright (2015) American Chemical Society

2,3-bis(4-(phenyl(4-(1,2,2-triphenylvinyl) phenyl)amino)phenyl) fumaronitrile (abbreviated as TTF) is a typical AIE luminogen with extended π -conjugation, which makes it possess large multiphoton absorption cross-section and other nonlinear optical effects, as well as emit far red/NIR light upon excitation [27, 53, 54]. Figure 18.9a shows the molecular structure of TTF [54]. It is a typical donor- π -acceptor- π -donor structure, which is helpful to the multiphoton absorption process [53, 54]. The absorption spectra of TTF in chloroform and toluene are centered at 515 and 495 nm, respectively (Fig. 18.9b). The red-shift of the absorption maximum

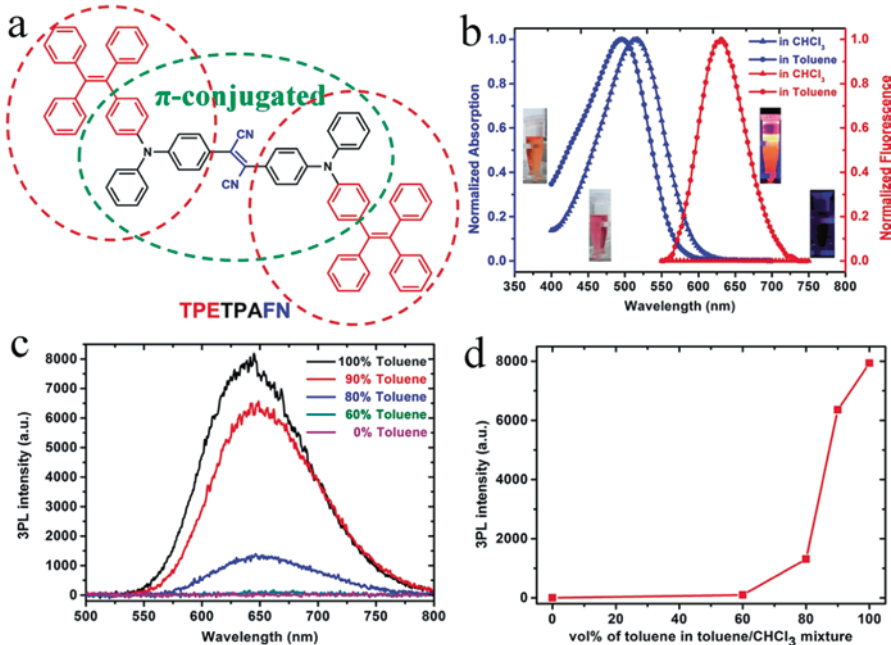


Fig. 18.9 (a) Molecular structure of TTF. (b) Linear absorption and emission spectra of TTF in chloroform and toluene. Insets: photographs showing chloroform and toluene solution of TTF under visible light (left) and ultraviolet light excitation (right). (c) Three-photon fluorescence from TTF in the chloroform/toluene mixture (1×10^{-3} M, in a glass capillary tube) with various volume ratios of toluene (excited by a femtosecond laser at 1560 nm). (d) Variations of three-photon fluorescence of TTF with volume ratio of toluene in the chloroform/toluene mixture. Adapted with permission from [54]. Copyright (2015) John Wiley & Sons Group

of TTF in chloroform was attributed to intramolecular charge transfer (ICT) character [54, 55]. Due to the twisted intramolecular charge transfer (TICT) phenomenon [56], TTF shows bright fluorescence in toluene, but is almost non-fluorescent in chloroform. By using 1560 nm fs laser for excitation, Qian et al. observed the three-photon fluorescence of TTF in the chloroform/toluene mixture (Fig. 18.6c) [54]. In this process, the TTF molecules absorbed three photons simultaneously and the excited TTF molecule was finally relaxed to the lowest excited electronic-vibrational state(s), from which the fluorescence emission occurred [54]. The intensity of three-photon fluorescence gradually increased, accompanied by blue-shifted peak emission wavelength, with increasing fraction of toluene (Fig. 18.6d) [54].

Li et al. [57] then reported the synthesis of TTF-nanodots by encapsulating TTF with 1,2-distearoyl-sn-glycero-3-phosphoethanolamine-*N*-methoxy-(polyethylene glycol)-2000 (DSPE-mPEG₂₀₀₀) and realized long-term three-photon fluorescence imaging of TTF-nanodots in zebrafish. The synthesis protocol of TTF-nanodots was shown in Fig. 18.10a and the obtained nanodots exhibited a spherical shape with an average diameter of 25 nm (Fig. 18.10b).

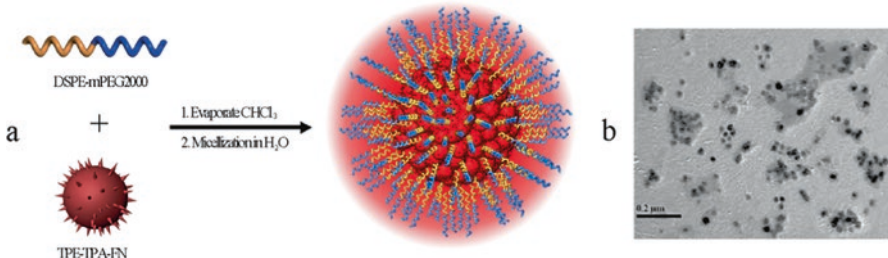


Fig. 18.10 (a) Schematic illustration of the preparation process of TTF-nanodots. (b) A typical TEM image of TTF-nanodots. Adapted with permission from [57]. Copyright (2016) Tsinghua University Press and Springer-Verlag Berlin Heidelberg

The toxicity assessments including cell apoptosis and expression of apoptosis-related genes demonstrated that the TTF-nanodots had no significant toxic to zebrafish, which was beneficial for the bioimaging applications [57]. The embryos of zebrafish were microinjected with TTF-nanodots and were then imaged at different growth stages with a three-photon fluorescence microscope equipped with a 1560 nm fs laser (Fig. 18.11a) [57]. The 1560 nm fs laser scanned from top to bottom of the zebrafish, obtaining one image at each focal plane during the imaging process [57]. The three-photon fluorescence images of zebrafish were then reconstructed by stacking together the images collected from the whole focal planes (Fig. 18.11b).

Figure 18.12 shows the bright field and three-photon fluorescence images of zebrafish after treated with TTF-nanodots for 6, 48, 96, and 120 h. The green points (pseudo-color) refer to the three-photon fluorescence signals of TTF-nanodots. The distribution of TTF-nanodots in zebrafish can be monitored and at the same time reflect some vital movement patterns of the treated zebrafish. The zebrafish embryo at 6 h was at a critical stage for the differentiation process, entering the shield-stage [58]. After incubated with embryos of zebrafish for 6 h, the TTF-nanodots accumulated not only at the yolk, but also at the surrounding tissues. These results demonstrated that TTF-nanodots could be transferred from yolk to newborn tissue. At 48 and 96 h after microinjection of TTF-nanodots, the three-photon fluorescence signals in zebrafish remained very bright, illustrating that the TTF-nanodots were chemically and optically stable in zebrafish, which can be tracked *in vivo* for a long period of time [57]. After 120 h, the density of TTF-nanodots in zebrafish decreased significantly due to the metabolism and excretion process of zebrafish. However, the signals could still be discriminated by the three-photon microscope by virtue of its imaging capability [57].

One region of interest in the zebrafish (marked as green in Fig. 18.13a) was continuously scanned with a 1560 nm fs laser to assess the photostability of TTF-nanodots. The corresponding three-photon fluorescence image was collected every 2 min. Figure 18.13b, c show the images of the region of interest at 0 and 60 min. Most of the three-photon fluorescence signals from the TTF-nanodots were detected and the intensity of the signal reduced by 40% even after continuously being

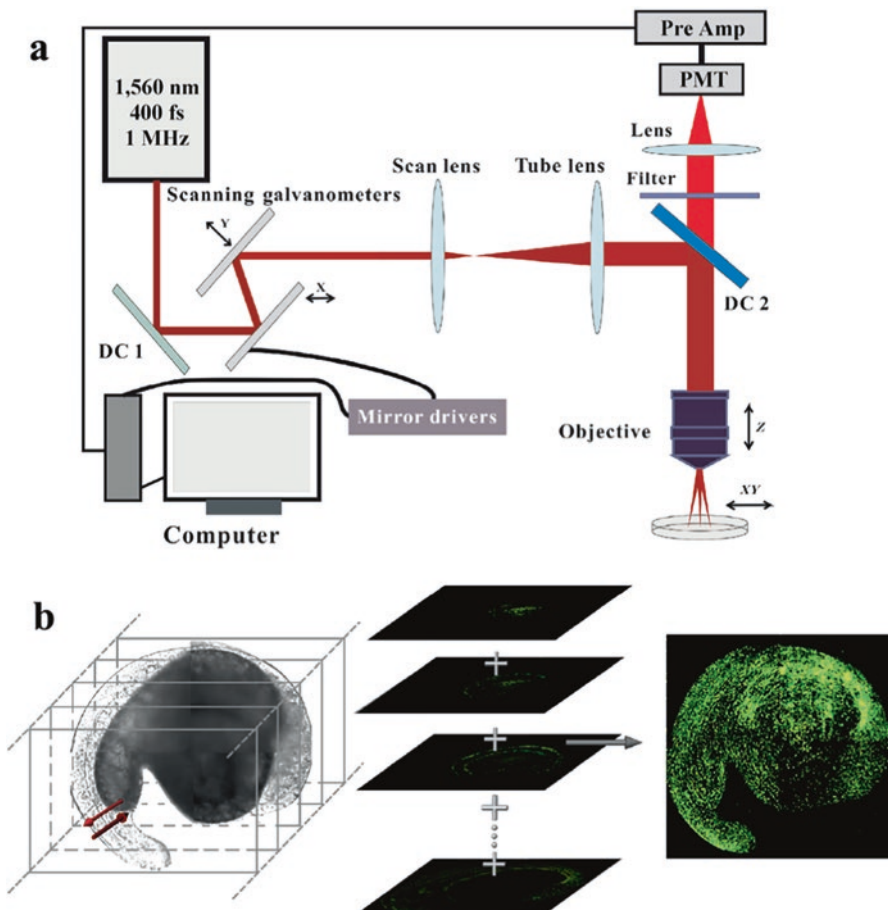
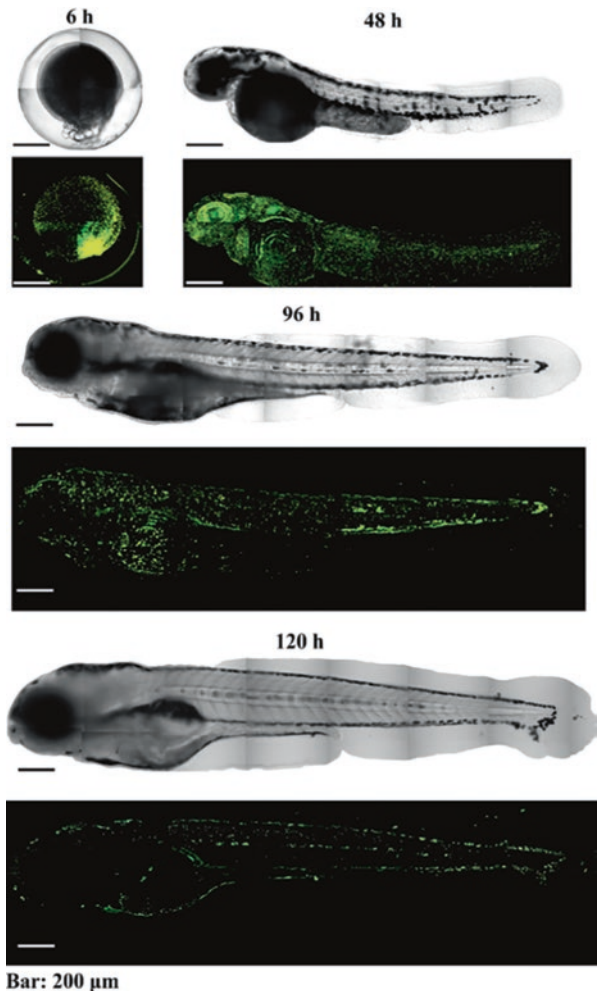


Fig. 18.11 (a) Schematic illustration of the three-photon fluorescence imaging system used to image zebrafish microinjected with TTF-nanodots. DC dichroic mirror. (b) Schematic illustration of three-photon fluorescence signal-stacked imaging of zebrafish. Adapted with permission from [57]. Copyright (2016) Tsinghua University Press and Springer-Verlag Berlin Heidelberg

scanned with a 1560 nm fs laser for 60 min (Fig. 18.13d). These results demonstrate that the TTF-nanodots are highly resistant to photobleaching under the exposure of 1560 nm fs excitation making them useful for long-term imaging and monitoring the growth of zebrafish [57].

In another work, Zhu et al. [59] used nanographene oxide (NGO) as a surface modification agent to encapsulate TTF nanoparticles (Fig. 18.14a). The acquired NGO-modified TTF nanoparticles (TTF-NGO NPs) showed very good stability in aqueous dispersion, and their size could be tuned by controlling the amount of added NGO. In the experiments, the NGO was synthesized with a modified Hummer's method [60–62], with an average size of 30 nm (Fig. 18.14b). The TTF was dissolved in tetrahydrofuran (THF), and then mixed with aqueous dispersion of NGO

Fig. 18.12 Bright field and three-photon fluorescence images of zebrafish at 6, 48, 96, and 120 h after microinjection of TTF-nanodots excited by a 1560 nm-fs laser. Adapted with permission from [57]. Copyright (2016) Tsinghua University Press and Springer-Verlag Berlin Heidelberg



to keep a final water volume fraction of 80 vol% [59]. After being dialyzed in water with an 8–14 kDa cut-off cellulose membrane for 50 h to remove THF, the solution was centrifuged at a certain speed to remove the excess NGO, and final TTF-NGO NPs were prepared [59].

By controlling the quantity of NGO, the size of the TTF-NGO NPs could be tuned [59]. Figure 18.15 shows the TEM images of TTF-NGO NPs ($[TTF] = 0.1 \text{ mM}$) with different quantities of NGO. The average diameter of the TTF-NGO NPs was 400 nm ($[NGO] = 5 \mu\text{g/mL}$), 300 nm ($[NGO] = 10 \mu\text{g/mL}$), and 200 nm ($[NGO] = 20 \mu\text{g/mL}$), respectively (Fig. 18.15a–c). The size of TTF-NGO NPs could also be tuned by changing the concentration of TTF (before dialysis and centrifugation) while keeping the quantity of NGO the same. The average diameter of TTF-NGO NPs ($[TTF] = 0.01 \text{ mM}$ and $[NGO] = 10 \mu\text{g/mL}$) was $\sim 100 \text{ nm}$ (Fig. 18.15d), which was

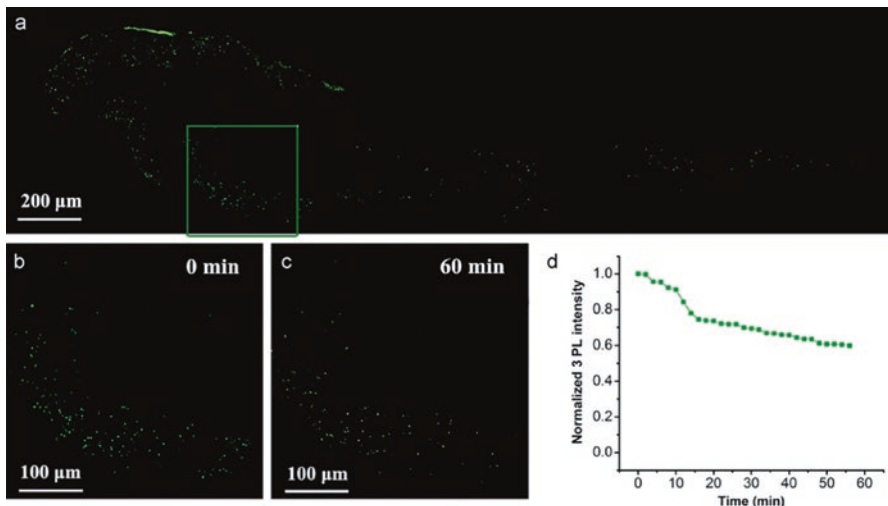


Fig. 18.13 (a) A three-photon fluorescence image of zebrafish at one depth (48 h post-microinjection) under excitation with the 1560 nm fs laser. The marked region was selected for assessing the photostability of TTF-nanodots under fs-excitation. Three-photon fluorescence images of the selected region at (b) 0 and (c) 60 min after fs laser scanning. (d) Three-photon fluorescence loss (%) of TTF-nanodots in the selected region with increasing scanning time with the 1560 nm fs laser. Adapted with permission from [57]. Copyright (2016) Tsinghua University Press and Springer-Verlag Berlin Heidelberg

much smaller than that of TTF-NGO NPs ($[TTF] = 0.1 \text{ mM}$ and $[NGO] = 10 \mu\text{g/mL}$), as shown in Fig. 18.15c [59].

The TTF-NGO NPs were microinjected into the embryos of zebrafish and three-photon fluorescence imaging of the zebrafish was realized after being cultured for 48 h [59]. As shown in Fig. 18.16, the TTF-NGO NPs uniformly distributed in the zebrafish with no significant aggregation of the TTF-NGO NPs based on the fact that no abnormally bright fluorescent spots were observed. These results indicated the TTF-NGO NPs were chemically and optically stable in the zebrafish and can be used as promising bioprobes for in vivo functional imaging in the future [59].

18.4 AIEgens for Three-Photon Fluorescence Imaging in Mice

The deep tissue imaging capability, high spatial resolution, and low thermal damage to biological samples make the three-photon fluorescence imaging technique very useful for brain imaging of small animals [54, 63–65]. By using TTF-nanodots as fluorescent probes, Qian et al. [54] realized three-photon *in vivo* microscopy imaging of the brain of mice. In the experiments, BALB/c mice were intravenously injected with suspensions of TTF-dots (with 20 wt% TTF loading, 1 mg mL^{-1} in $1\times$

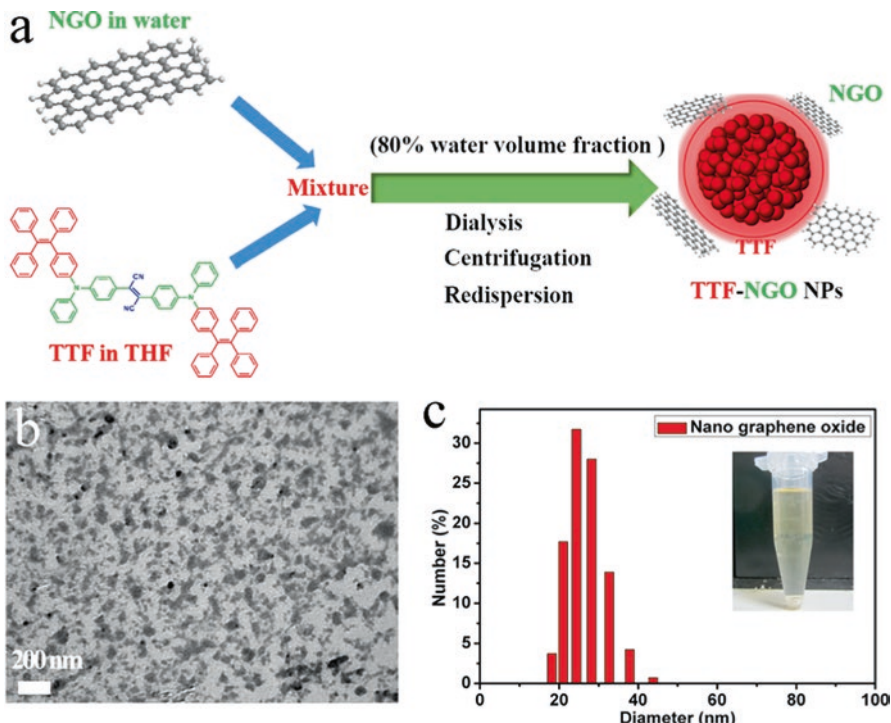


Fig. 18.14 (a) Schematic Illustration for the Synthesis of TTF-NGO NPs. (b) TEM image of NGO. (c) DLS number-weighted diameter of NGO. Inset: Photograph of an aqueous dispersion of NGO under daylight. Adapted with permission from [59]. Copyright (2016) American Chemical Society

Fig. 18.15 TEM images of TTF-NGO NPs ($[TTF] = 0.1 \text{ mM}$), with varying quantities of added NGO: (a) $5 \mu\text{g/mL}$ NGO, (b) $10 \mu\text{g/mL}$ NGO, and (c) $20 \mu\text{g/mL}$ NGO. (d) TEM image of TTF-NGO NPs ($[TTF] = 0.01 \text{ mM}$), with the addition of $10 \mu\text{g/mL}$ NGO. Scale bars in TEM images: 500 nm . Adapted with permission from [59]. Copyright (2016) American Chemical Society

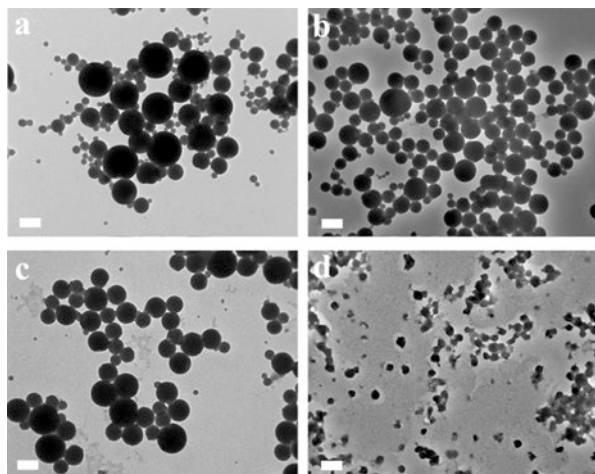
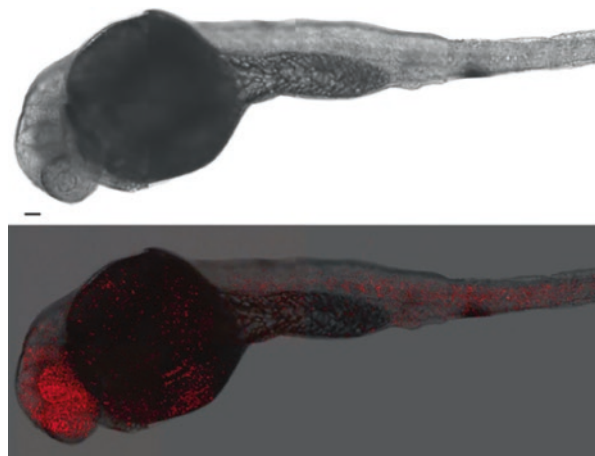


Fig. 18.16 (a)

Transmission image and (b) merge of transmission and 3PL images of zebrafish injected with TTF-NGO NPs. Scale bar: 500 nm. Adapted with permission from [59]. Copyright (2016) American Chemical Society



PBS, 250 μ L solutions per mouse) via their tail vein. The mice were then anesthetized with pentobarbital, and their skulls were opened up through microsurgery. An upright 3PFM (1560 nm fs laser excited) was adopted for the imaging of blood vasculature in the mouse brain, following a well-developed proposal [27, 54, 62]. Deuteroxide was smeared between the long work distance (2 mm) water-immersed objective (XLPLN25XWMP2, Olympus, 25 \times 1.05 NA) and the top of the cover slide [54]. The distinct three-photon fluorescence from the intravenously injected TTF-nanodots is helpful to reveal the vascular architecture in the mouse brain at different vertical depths along with some tiny structure of capillary vessels. The three-photon fluorescence imaging depth reached as deep as 550 μ m in the mouse brain [54] (Fig. 18.17).

Furthermore, Zhang et al. [63] reported a red emissive AIE dye named TPEPT with tetraphenylethene (TPE) as the donor group and [1,2,5]thiadiazolo[3,4-c]pyridine (PT) as the acceptor group (Fig. 18.16a) [63, 66]. Nanoparticles of TPEPT (TPEPT-NPs) were then prepared by encapsulating TPEPT with 1,2-distearoyl-sn-glycero-3-phosphoethanolamine-*N*-methoxy-(polyethylene glycol)-5000 (DSPE-mPEG₅₀₀₀) following a facile micellization process (Figs. 18.16b and 18.18) [63].

Figure 18.19a shows a typical TEM image of the TPEPT-NPs, revealing an average diameter of 45 nm. The absorption (black line) and fluorescence (red line) spectra of TPEPT-NPs under 520 nm excitation are presented in Fig. 18.19b. The one-photon absorption peak of TPEPT-NPs was located at 520 nm and the fluorescence peak was at 654 nm, giving a deep red emission [63].

The three-photon fluorescence spectrum of the TPEPT-NPs was centered at 680 nm (Fig. 18.20), which agreed well with the one-photon fluorescence spectrum in Fig. 18.19b. The power dependence relationship of TPEPT-NPs under a 1550 nm fs excitation was shown in Fig. 18.20, and the fluorescence intensity of TPEPT-NPs exhibited linear proportion to the cubic of the excitation intensity, indicating that the main nonlinear optical process was three-photon fluorescence [63].

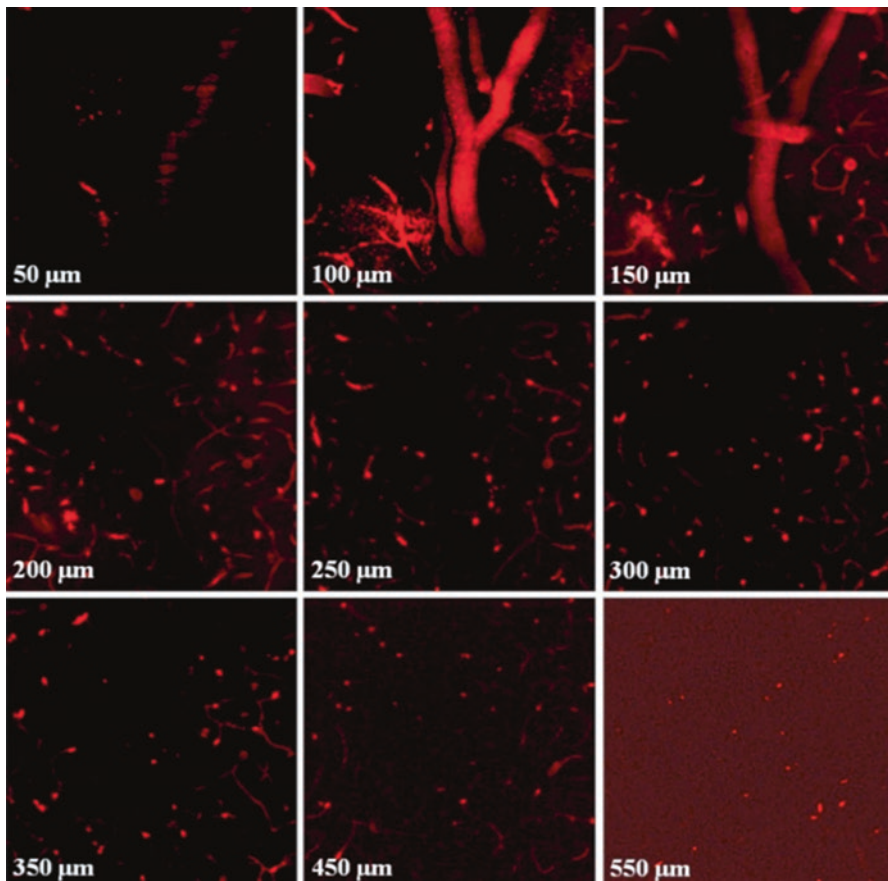


Fig. 18.17 3PFM imaging of brain blood vessels of a mouse (intravenously injected with TTF-nanodots) at different depths. All the images were taken under the 3PFM equipped with the 1560 nm fs laser. Adapted with permission from [54]. Copyright (2015) John Wiley & Sons Group

The three-photon absorption cross-section of TPEPT molecules at 1550 nm was $6.33 \times 10^{-78} \text{ cm}^6 \text{ s}^2$, holding great potential for three-photon fluorescence imaging. Zhang et al. realized three-photon imaging of TPEPT NPs in the brain blood vessels of mice, using an upright three-photon fluorescence microscopy coupled with a 1550 nm fs laser as the excitation light [63]. The three-photon fluorescence signal of TPEPT-NPs can clearly be observed to reveal the structure of brain blood vessels of mice at different depths (Fig. 18.21a–g). In the imaging depth from 0 μm (Fig. 18.21a) to 300 μm (Fig. 18.21d), some coarser vessels were observed, while only capillaries were found in the depth range from 400 μm (Fig. 18.21e) to 505 μm (Fig. 18.21g). Figure 18.21h shows a stacked three-photon fluorescence image from a depth of 0–505 μm, revealing the complex structures of the blood vessels in the brain of mice. A 3D mixed image of the TPEPT-NPs in the blood vessels of the brain of a mouse was reconstructed in Fig. 18.21i to show the space structures. The deep tissue imag-

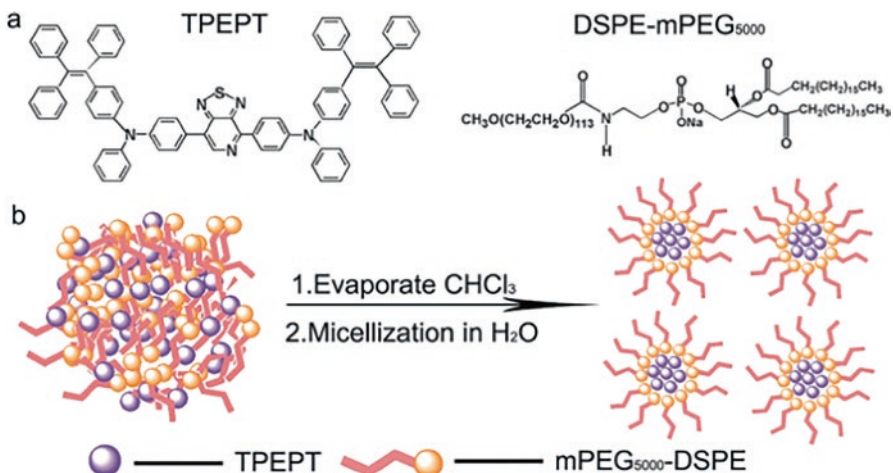


Fig. 18.18 (a) Chemical structures of the compounds forming TPEPT-NPs. (b) A schematic illustration of the preparation of TPEPT-NPs. Adapted with permission from [63]. Copyright (2017) The Royal Society of Chemistry

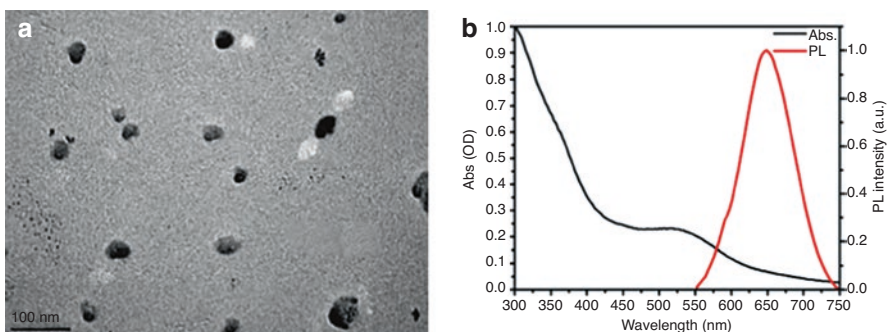


Fig. 18.19 (a) TEM image of TPEPT-NPs (b) absorption and fluorescence spectra of TPEPT-NPs, $\lambda_{\text{excitation}} = 520 \text{ nm}$. Adapted with permission from [63]. Copyright (2017) The Royal Society of Chemistry

ing capability, high spatial resolution, high signal-to-noise ratio, and low thermal damage to biological samples make TPEPT-NPs-based three-photon fluorescence imaging very useful for brain vascular imaging of small animals [63].

Wang et al. [64] investigated the three-photon fluorescence properties of 2,3-bis(4'-diphenylamino)-[1,1'-biphenyl]-4-yl fumaronitrile (TPATCN, Fig. 18.22). The TPATCN molecular has a donor–acceptor–donor (D-A-D) structure, with triphenylamine (TPA) as the donor and diphenylfumaronitrile (DBFN) as the acceptor, and this configuration would endow it with narrow band gap [64, 67]. TPA has strong light absorption and DBFN possesses high fluorescence efficiency [64, 68, 69].

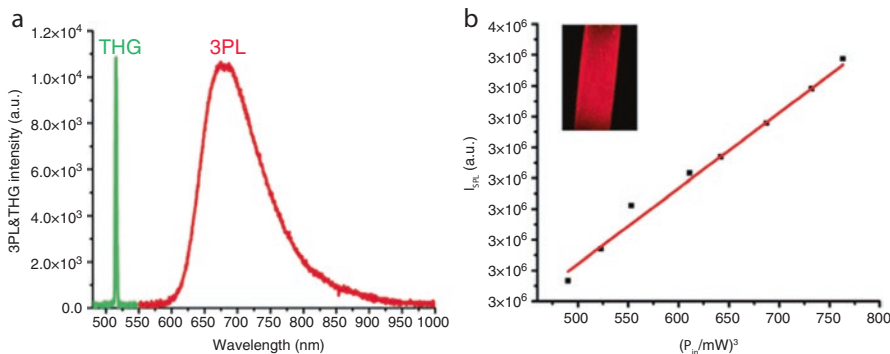


Fig. 18.20 (a) Nonlinear response of TPEPT-NPs. (b) Power dependence relationship of TPEPT-NPs. Inset: three-photon fluorescence imaging of an aqueous dispersion of TPEPT-NPs in a glass capillary tube under 1550 nm fs laser excitation. Adapted with permission from [63]. Copyright (2017) The Royal Society of Chemistry

Therefore, the D-A-D-type luminogen TPATCN is designed to show NIR fluorescence [70].

Aqueously dispersible TPATCN NPs were obtained via a modified nanoprecipitation method by utilizing TPATCN molecules as the core and F127 as the matrix (Fig. 18.23a) [64]. The TPATCN NPs exhibited an averaged hydrodynamic diameter of 31.4 nm (Fig. 18.23b). The TEM image of the TPATCN NPs reveals a spherical shape (Fig. 18.23c). The dispersion of TPATCN NPs gave an orange yellow appearance under daylight with an extinction peak around 440 nm (Fig. 18.23d). Under ultraviolet (UV) lamp irradiation, bright emission was observed with a fluorescence peak at 642 nm (Fig. 18.23e). The lifetime of TPATCN NPs was measured via a time-correlated single-photon counting (TCSPC) system, under the 1550 nm fs laser excitation. As shown in Fig. 18.20f, TPATCN NPs displayed a short lifetime of 2.25 ± 0.06 ns, indicating the fast emissive rate of TPATCN NPs [64].

The three-photon fluorescence spectrum of the aqueous dispersion of TPATCN NPs was measured using a 1550 nm fs laser as the excitation light. An emission peak at 650 nm was observed and the envelope of the three-photon fluorescence spectrum (Fig. 18.24a) was similar to the one-photon excited fluorescence spectrum (Fig. 18.23e). The logarithm of the fluorescence intensity of TPATCN NPs showed linear proportion to the logarithm of the excitation power, with a slope of 2.81 (Fig. 18.24b), indicating that the main nonlinear optical process was three-photon fluorescence. The three-photon absorption cross-section of the TPATCN molecule in chloroform at 1500 nm wavelength was measured to be $5.77 \times 10^{-79} \text{ cm}^6 \text{ s}^2$, which was very close to that of bright quantum dots (QDs) [64, 71].

The *in vivo* three-photon fluorescence imaging of the brain vasculature of mice intravenously injected with TPATCN NPs was performed under the 1550 nm fs laser excitation [64]. The three-photon fluorescence signals of TPATCN NPs in the brain blood vessels of mice were clearly observed in the depth of 0–200 μm (Fig. 18.25a–c). The SBR of the imaging was calculated by drawing a line across the

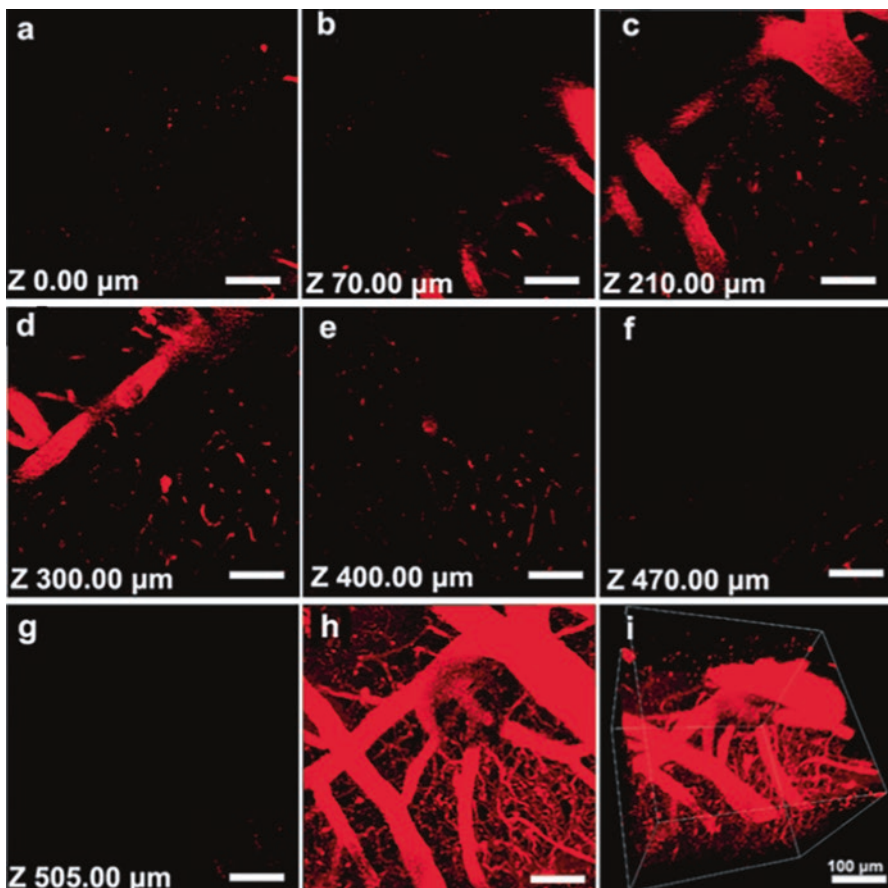
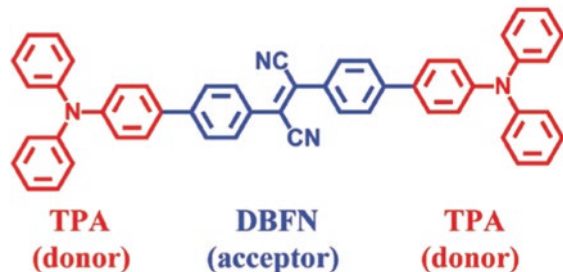


Fig. 18.21 3PL imaging of brain blood vessels of a mouse treated with TPEPT-NPs. Individual images taken at the depths of (a) 0 mm, (b) 70 mm, (c) 210 mm, (d) 300 mm, (e) 400 mm, (f) 470 mm, and (g) 505 mm. (h) A stacked three-photon fluorescence image from a depth of 0–505 mm. (i) A reconstructed 3D image showing the distribution of the TPEPT-NPs in blood vessels of the mouse. Adapted with permission from [63]. Copyright (2017) The Royal Society of Chemistry

Fig. 18.22 Chemical structure of TPATCN. Adapted with permission from [64]. Copyright (2017) John Wiley & Sons Group



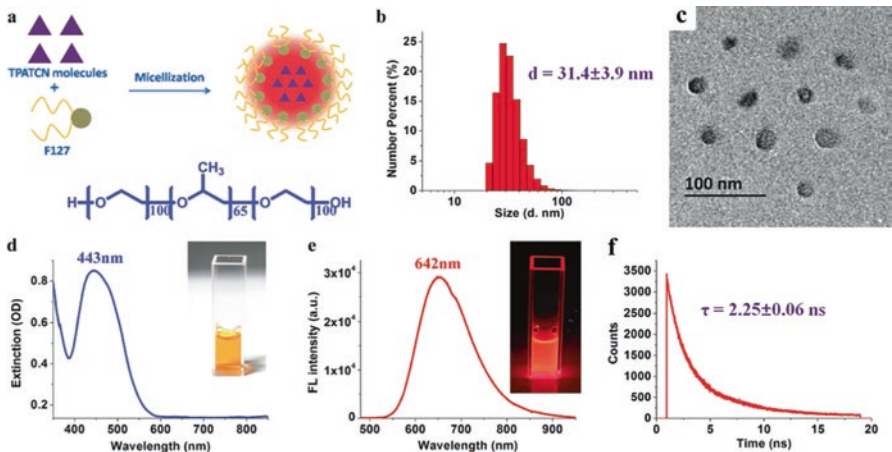


Fig. 18.23 (a) A scheme showing the encapsulation routine of TPATCN NPs. (b) The number-weighted hydrodynamic diameter of TPATCN NPs obtained by DLS. (c) A TEM image of TPATCN NPs. (d) The extinction spectrum of TPATCN NPs. Inset: The photograph of TPATCN NPs in aqueous dispersion under daylight. (e) The fluorescence spectrum of TPATCN NPs under a 450 nm laser excitation. Inset: The photograph of TPATCN NPs in aqueous dispersion under a UV lamp irradiation. (f) A time-resolved decay profile of the 3PF signals from TPATCN NPs. Adapted with permission from [64]. Copyright (2017) John Wiley & Sons Group

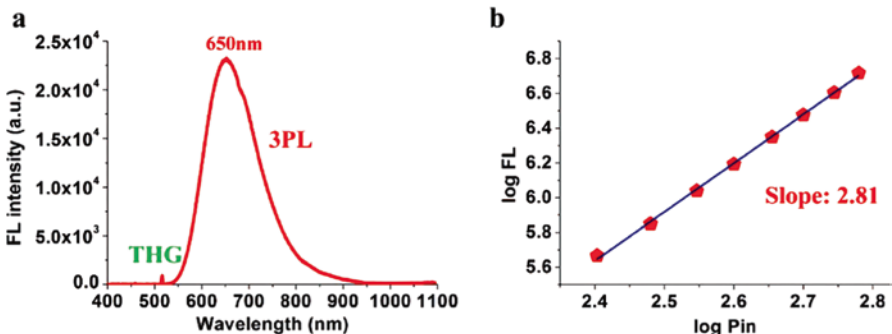


Fig. 18.24 (a) The nonlinear optical response of TPATCN NPs, under the 1550 nm fs laser excitation. (b) The excitation power dependence relationship of the fluorescence from TPATCN NPs, under the 1550 nm fs laser irradiation. P_{in} stands for input power. Adapted with permission from [64]. Copyright (2017) John Wiley & Sons Group

blood vessel and plotting the pixel intensity distribution on the line [64, 72]. A SBR value was obtained by analyzing the three-photon fluorescence image of TPATCN NPs in the depth of 200 μm . By increasing the excitation power and the photomultiplier tube (PMT) bias voltage to compensate for the three-photon fluorescence signal loss, clear imaging was still realizable (Fig. 18.25d–g). However, when the imaging depth was over 700 μm , the three-photon fluorescence from the focal point was therefore not so distinct, and the pixels in the obtained image were blurred,

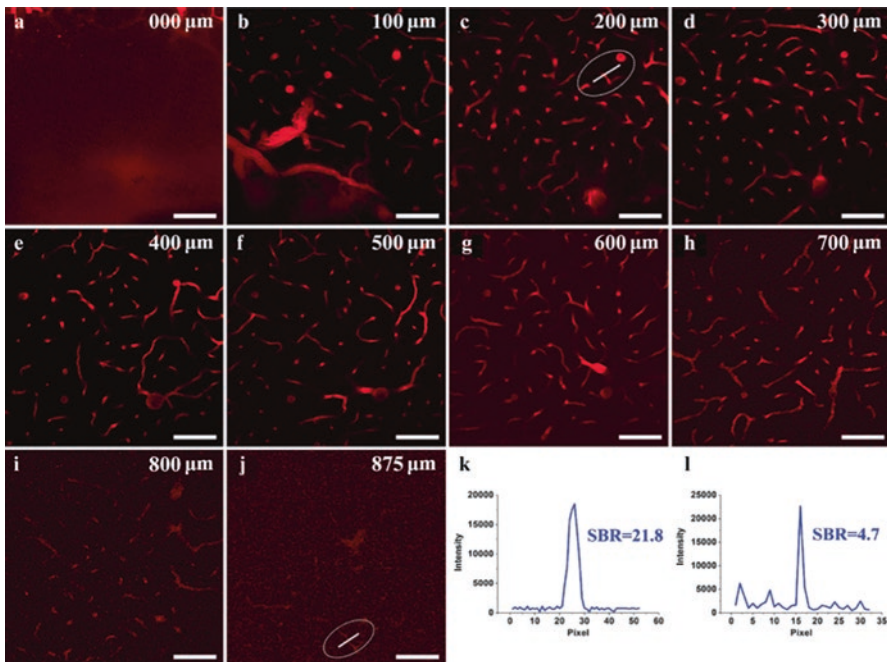


Fig. 18.25 In vivo three-photon fluorescence images of the brain blood vessels of a mouse intravenously injected with TPATCN NPs. (a–j) Three-photon fluorescence images at various vertical depths, 0–875 μm . SBR of 3PF images at (k) 200 μm and (l) 875 μm . Scale bar: 100 μm . Adapted with permission from [64]. Copyright (2017) John Wiley & Sons Group

leaving only a few blood vessels still distinguishable (Fig. 18.25i, j) [64]. These results were caused by the strong scattering of excitation laser beam in the brain tissue. Nevertheless, a SBR value of 4.7 was obtained from the three-photon fluorescence image at 875 μm [64].

Although 3PFM imaging of AIEgens in the brain of mice has been carried out, the above-mentioned examples still require craniotomy and cranial windows or skull-thinning techniques due to distinct photon scattering of the excitation laser in the skull [65]. The craniotomy treatment of mice may destroy the integrity of cerebral vasculature, causing inflammation on the brain tissue. Recently, Wang et al. [65] reported through-skull three-photon fluorescence imaging of mouse cerebral vasculature without craniotomy and skull-thinning using a deep-red emissive AIEgen as the probe. Based on the reported AIEgen of 2,3-dicyano-5,6-diphenylpyrazine (DCDPP) [73], which shows strong electron-accepting ability, a new AIEgen named 5,6-bis(4'-(diphenylamino)-[1,1'-biphenyl]-4-yl)pyrazine-2,3-dicarbonitrile (DCDPP-2TPA) was obtained by modifying DCDPP with a strong electron donor of triphenylamine (TPA) following the synthetic route shown in Fig. 18.26 [65].

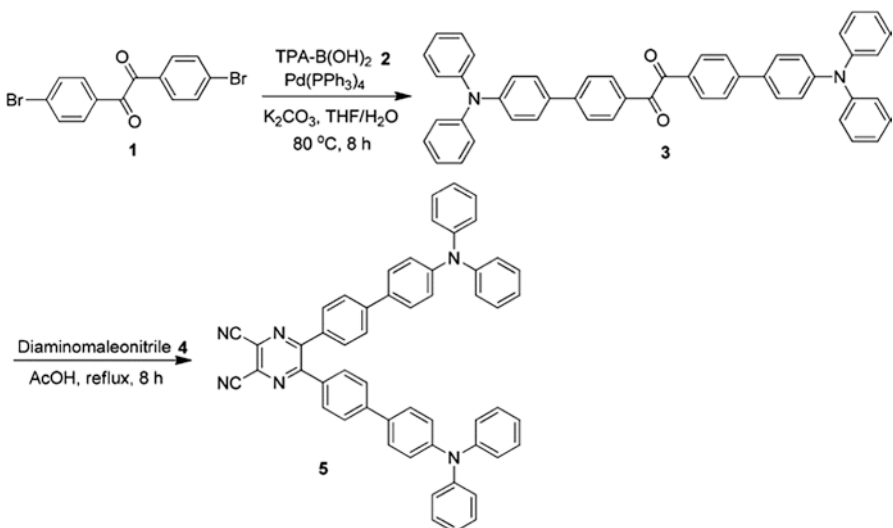


Fig. 18.26 Synthetic route to AIEgen of DCDPP-2TPA. Adapted with permission from [65]. Copyright (2017) American Chemical Society

Aqueously dispersible DCDPP-2TPA NPs were then prepared by encapsulating DCDPP-2TPA with amphiphilic polymer (F127) (Fig. 18.27a). The average diameter of the DCDPP-2TPA NPs was 29 nm according to the TEM image (Fig. 18.27b). The DCDPP-2TPA NPs showed an absorption peak at 440 nm (Fig. 18.2c, blue line) and an emission peak at 642 nm (Fig. 18.27c). The three-photon fluorescence spectrum of DCDPP-2TPA NPs excited by a 1550 nm fs laser exhibited similar trends with a peak at 650 nm (Fig. 18.27d). The logarithm of the fluorescence intensity of DCDPP-2TPA NPs and the logarithm of the excitation power (P_{in}) had a good linear relationship with a slope of 2.84 (Fig. 18.27e), indicating that the main nonlinear optical process was three-photon fluorescence [65].

DCDPP-2TPA NPs were further used for *in vivo* brain vasculature imaging of mice with intact skulls under the same 1550 nm fs laser excitation (Fig. 18.28a) [65]. On the cranium layer in the depth range of 0–100 μm , no fluorescence signal was observed since the intravenously injected DCDPP-2TPA NPs were not delivered into the skull of the mouse (Fig. 18.28b–d). The three-photon fluorescence signal of DCDPP-2TPA NPs appeared when the imaging depth reached 150 μm and the blood vessels in the brain were revealed. To evaluate the imaging quality, a line was drawn across the capillary, and the pixel intensities on it were plotted (Fig. 18.28e, i) [65]. The blood vessels as small as 2.0 μm could be recognized at 150 μm beneath the skull with a SBR of 20.4 [65]. When further increasing the focusing depth, the quality of images began to deteriorate due to the photon scattering of skull and brain tissues (Fig. 18.28f, g) [65]. An *in vivo* penetration depth of 300 μm beneath the skull was achieved on the mouse with intact skull, although the SBR value was relatively low (Fig. 18.28h, j). The 3D reconstruction of the brain vasculature was sub-

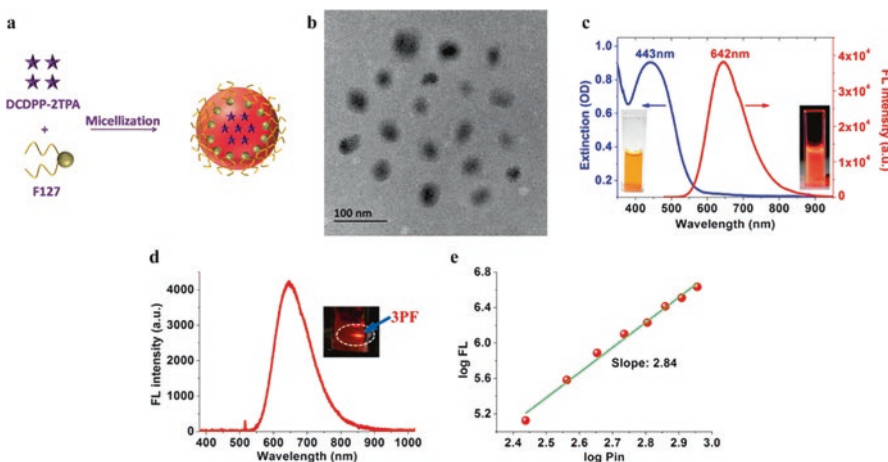


Fig. 18.27 (a) Synthesis scheme of DCDPP-2TPA NPs, with F127 as the encapsulation matrix. (b) TEM image of DCDPP-2TPA NPs. Scale bar: 100 nm. (c) Extinction spectrum (blue) and fluorescence spectrum (red) of DCDPP-2TPA NPs in aqueous dispersion; 0.03 mg mL^{-1} of DCDPP-2TPA. Excitation wavelength = 450 nm. Inset: Photographs of DCDPP-2TPA NPs under daylight and under a UV lamp irradiation. (d) Nonlinear optical response of DCDPP-2TPA NPs in aqueous dispersion, under the 1550 nm fs laser excitation. Inset: Photograph showing the red 3PF signals in the aqueous dispersion of DCDPP-2TPA NPs. (e) Power dependence relationship of the fluorescence from DCDPP-2TPA NPs, under the same 1550 nm fs laser excitation. Adapted with permission from [65]. Copyright (2017) American Chemical Society

sequently built (Fig. 18.4k) in which the major blood vessels and some small capillaries were clearly distinguished [65]. More areas of the mouse brain were further observed with three-photon fluorescence imaging, and one of them was selectively shown in Fig. 18.28l. The brain blood flow velocity was also noninvasively measured with the through-skull three-photon fluorescence imaging. A line scan along the capillary was used to detect the RBCs' flow, and its instantaneous velocity (dx/dt) was calculated to be 2.4 mm s^{-1} (Fig. 18.29). The bright three-photon fluorescence signals from DCDPP-2TPA NPs, together with their good photostability and biocompatibility, contributed to the successful imaging of mouse brain. Through-skull three-photon fluorescence imaging has great meanings to non-invasive study of brain structure and functions, which requires high spatial resolution and certain penetration depth [65].

18.5 Summary and Perspectives

In this chapter, recent advances in AIEgens assisted three-photon fluorescence bioimaging of cells, zebrafish embryos, and mice are summarized. Even this short chapter has revealed the versatility of AIEgens for three-photon fluorescence

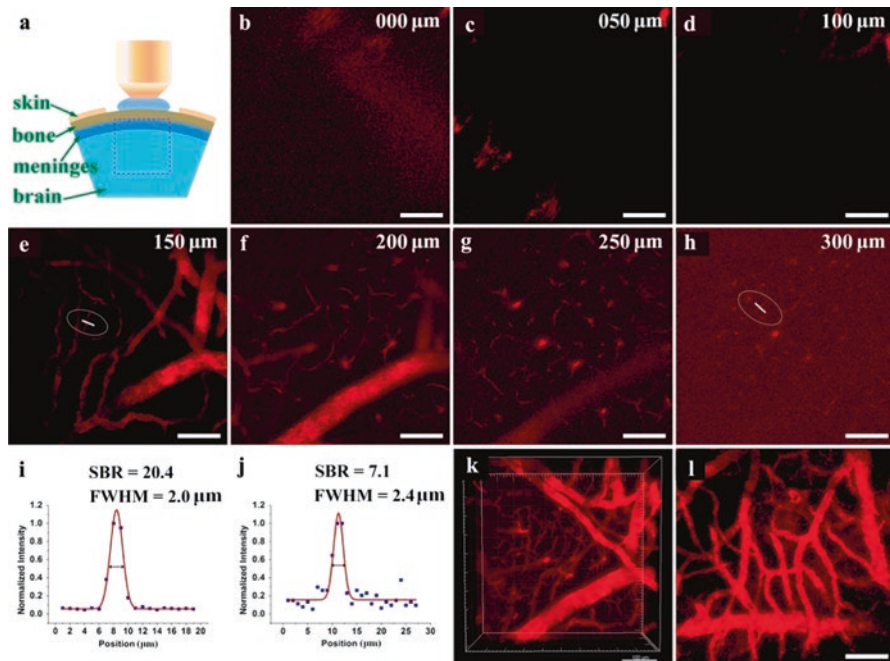


Fig. 18.28 In vivo three-photon fluorescence imaging of the brain blood vessels on a mouse with intact skull. **(a)** Demonstration of the imaging area in the mouse brain. **(b-h)** Three-photon fluorescence images of the blood vessels at various vertical depths, 0–300 μm. **(i, j)** Values of fwhm of blood vessels and SBR analysis of three-photon fluorescence images at 150 μm **(i)** and 300 μm **(j)**. **(k)** 3D reconstruction of the blood vessels in mouse brain, 150–300 μm. **(l)** Three-photon fluorescence image of the blood vessels at another area in mouse brain. Excitation = 1550 nm fs laser (1 MHz). Scale bar: 100 μm. Adapted with permission from [65]. Copyright (2017) American Chemical Society

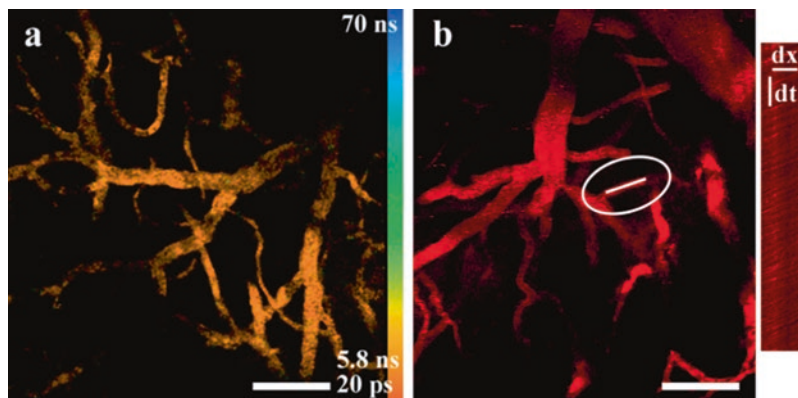


Fig. 18.29 In vivo functional imaging of the brain blood vessels on a mouse with intact skull. **(a)** 3PF lifetime image of the blood vessels. **(b)** Measurement of the blood flow velocity ($\frac{dx}{dt}$). Excitation = 1550 nm fs laser (1 MHz). Scale bar: 100 μm. Adapted with permission from [65]. Copyright (2017) American Chemical Society

bioimaging. With so many synthetic approaches already reported, and more to be developed, there will be many opportunities for developing various new AIEgens with well-defined fluorescence properties and tailor-made structures desirable for bioimaging. However, the applications of AIEgens for three-photon fluorescence bioimaging are still at its early stage with many important issues remained to be addressed.

The second near-infrared window (NIR-II, 1000–1700 nm) has proven more desirable than visible (450–750 nm) and traditional NIR-I imaging (750–900 nm) due to reduced photon scattering, deeper tissue penetration, and lower autofluorescence. AIEgens with large three-photon absorption cross-section in the NIR-II region are required to achieve high fluorescence quantum yield for advanced bioimaging. AIEgens with emission in the red and far-red regions are beneficial for deep-tissue imaging, since the red and far-red fluorescence is easy to come out from the tissue to be detected.

Like many other new biomedical technologies, there are concerns about the possible side effects derived from the use of AIEgens. Toxicity studies of AIEgens with different components, sizes, shapes, and surface coatings need to be investigated. Biodistribution studies of AIEgens in various animal models are also needed. The biomedical applications of the newly developed AIEgens would hardly be realized unless the potential hazards of them to human and other biological systems are carefully ascertained.

To obtain large imaging depth, the three-photon fluorescence imaging system still needs optimization. Since the scattering coefficients vary in different tissues, a concrete analysis of specific situations is required to confirm the optimized fs laser for excitation. The knowledge of the three-photon absorption cross-sections of AIEgens for lights with various wavelengths can serve as a guideline for the choosing of pulsed lasers. In the case of using NIR-II light, the lenses and mirrors need special coatings to obtain good transmittance or reflection. The physical parameters of the pulsed fs laser, such as the output power, the repetition frequency, and the duty cycle, may also have an impact on the quality of the three-photon fluorescence imaging.

Acknowledgments This work was partially supported by the National Natural Science Foundation of China (61735016), the Zhejiang Provincial Natural Science Foundation of China (LR17F050001), and the National Basic Research Program of China (973 Program; 2013CB834704).

References

1. Kowada T, Maeda H, Kikuchi K (2015) BODIPY-based probes for the fluorescence imaging of biomolecules in living cells. *Chem Soc Rev* 44:4953–4972
2. Tanenbaum ME, Gilbert LA, Qi LS et al (2014) A protein-tagging system for signal amplification in gene expression and fluorescence imaging. *Cell* 159:635–646
3. Hong G, Diao S, Chang J et al (2014) Through-skull fluorescence imaging of the brain in a new near-infrared window. *Nat Photon* 8:723–730

4. Prasad PN (2004) Introduction to biophotonics. John Wiley & Sons, New Jersey
5. Zhang Q, Piston DW, Goodman RH (2002) Regulation of corepressor function by nuclear NADH. *Science* 295:1895–1897
6. Rice WL, Kaplan DL, Georgakoudi I (2010) Two-photon microscopy for non-invasive, quantitative monitoring of stem cell differentiation. *PLoS One* 5:e10075
7. Kim HM, Cho BR (2009) Two-photon probes for intracellular free metal ions, acidic vesicles, and lipid rafts in live tissues. *Acc Chem Res* 42:863–872
8. Resch-Genger U, Grabolle M, Cavaliere-Jaricot S et al (2008) Quantum dots versus organic dyes as fluorescent labels. *Nat Methods* 5:763–775
9. Wang D, Chen J, Dai L (2015) Recent advances in graphene quantum dots for fluorescence bioimaging from cells through tissues to animals. Part Part Syst Charact 5:515–523
10. Wang D, Wang Z, Zhan Q et al (2017) Facile and scalable preparation of fluorescent carbon dots for multifunctional applications. *Engineering* 3:402–408
11. Mycek MA, Pogue BW (2003) Handbook of biomedical fluorescence. CRC Press, New York
12. Yan J, Estévez MC, Smith JE et al (2007) Dye-doped nanoparticles for bioanalysis. *Nano Today* 2:44–50
13. Qian J, Wang D, Cai F et al (2012) Photosensitizer encapsulated organically modified silica nanoparticles for direct two-photon photodynamic therapy and in vivo functional imaging. *Biomaterials* 33:4851–4860
14. Zhang Y, Qian J, Wang D et al (2013) Multifunctional gold nanorods with ultrahigh stability and tunability for in vivo fluorescence imaging, SERS detection, and photodynamic therapy. *Angew Chem Int Ed* 52:1148–1151
15. Kumar R, Roy I, Ohulchansky TY et al (2008) Covalently dye-linked, surface-controlled, and bioconjugated organically modified silica nanoparticles as targeted probes for optical imaging. *ACS Nano* 2:449–456
16. Qian J, Jiang L, Cai F et al (2011) Fluorescence-surface enhanced Raman scattering co-functionalized gold nanorods as near-infrared probes for purely optical in vivo imaging. *Biomaterials* 32:1602–1610
17. Wang D, Zhu L, Pu Y et al (2017) Transferrin-coated magnetic upconversion nanoparticles for efficient photodynamic therapy with near-infrared irradiation and luminescence bioimaging. *Nanoscale* 9:11214–11221
18. Birks JB (1970) Photophysics of aromatic molecules. John Wiley & Sons, London
19. Yuan WZ, Lu P, Chen S et al (2010) Changing the behavior of chromophores from aggregation-caused quenching to aggregation-induced emission: development of highly efficient light emitters in the solid state. *Adv Mater* 22:2159–2163
20. Qian J, Tang BZ (2017) AIE luminogens for bioimaging and theranostics: from organelles to animals. *Chem* 3:56–91
21. Luo J, Xie Z, Lam JW et al (2001) Aggregation-induced emission of 1-methyl-1, 2, 3, 4, 5-pentaphenylsilole. *Chem Commun* (28):1740–1741
22. Hong Y, Lam JW, Tang BZ (2011) Aggregation-induced emission. *Chem Soc Rev* 40:5361–5388
23. Zhao Z, Lam JW, Tang BZ (2012) Tetraphenylethene: a versatile AIE building block for the construction of efficient luminescent materials for organic light-emitting diodes. *J Mater Chem* 22:23726–23740
24. Chen J, Law CC, Lam JW et al (2003) Synthesis, light emission, nanoaggregation, and restricted intramolecular rotation of 1, 1-substituted 2, 3, 4, 5-tetraphenylsiloles. *Chem Mater* 15:1535–1546
25. He J, Xu B, Chen F et al (2009) Aggregation-induced emission in the crystals of 9, 10-distyrylanthracene derivatives: the essential role of restricted intramolecular torsion. *J Phys Chem C* 113:9892–9899
26. Wang D, Qian J, He S et al (2011) Aggregation-enhanced fluorescence in PEGylated phospholipid nanomicelles for in vivo imaging. *Biomaterials* 32:5880–5888
27. Wang D, Qian J, Qin W et al (2014) Biocompatible and photostable AIE dots with red emission for in vivo two-photon bioimaging. *Sci Rep* 4:4279

28. Jacques SL (2013) Optical properties of biological tissues: a review. *Phys Med Biol* 58:R37
29. Zipfel WR, Williams RM, Webb WW (2003) Nonlinear magic: multiphoton microscopy in the biosciences. *Nat Biotechnol* 21:1369–1377
30. Gao Y, Feng G, Jiang T et al (2015) Biocompatible nanoparticles based on diketo-pyrrolo-pyrrole (DPP) with aggregation-induced red/NIR emission for in vivo two-photon fluorescence imaging. *Adv Funct Mater* 25:2857–2866
31. Geng J, Goh CC, Qin W et al (2015) Silica shelled and block copolymer encapsulated red-emissive AIE nanoparticles with 50% quantum yield for two-photon excited vascular imaging. *Chem Commun* 51:13416–13419
32. Gu B, Wu W, Xu G et al (2017) Precise two-photon photodynamic therapy using an efficient photosensitizer with aggregation-induced emission characteristics. *Adv Mater* 29:1701076
33. Lou X, Zhao Z, Tang BZ (2016) Organic dots based on AIEngens for two-photon fluorescence bioimaging. *Small* 12:6430–6450
34. Wang Y, Hu R, Xi W et al (2015) Red emissive AIE nanodots with high two-photon absorption efficiency at 1040 nm for deep-tissue in vivo imaging. *Biomed Opt Express* 6:3783–3794
35. Wang Y, Zhang H, Alifu N, Qian J (2016) AIE nanoprobes for multi-photon in vivo bioimaging. In: Fujiki M, Liu B, Tang BZ (ed) Aggregation-induced emission: materials and applications, vol 2 (Chapter 10). ACS symposium series, vol 1227. ACS Publications, Washington, DC, pp 245–270. <https://doi.org/10.1021/bk-2016-1227.ch010>. ISBN13: 9780841231580. eISBN: 9780841231573. Publication date (Web): September 27, 2016. Copyright © 2016 American Chemical Society.
36. Horton NG, Wang K, Kobat D et al (2013) In vivo three-photon microscopy of subcortical structures within an intact mouse brain. *Nat Photon* 7:205–209
37. Mei J, Leung NL, Kwok RT et al (2015) Aggregation-induced emission: together we shine, united we soar! *Chem Rev* 115:11718–11940
38. Leung CWT, Hong Y, Chen S et al (2013) A photostable AIE luminogen for specific mitochondrial imaging and tracking. *J Am Chem Soc* 135:62–65
39. Leung CWT, Guo F, Hong Y et al (2015) Detection of oligomers and fibrils of α -synuclein by AIEngen with strong fluorescence. *Chem Commun* 51:1866–1869
40. Zhu Z, Leung CWT, Zhao X et al (2015) Using AIE luminogen for long-term and low-background three-photon microscopic functional bioimaging. *Sci Rep* 5:15189
41. Hell SW, Bahlmann K, Schrader M et al (1996) Three-photon excitation in fluorescence microscopy. *J Biomed Opt* 1:71–75
42. Nishikawa T, Edelstein D, Du XL et al (2000) Normalizing mitochondrial superoxide production blocks three pathways of hyperglycaemic damage. *Nature* 404:787–790
43. Chen IH, Chu SW, Sun CK (2002) Wavelength dependent damage in biological multi-photon confocal microscopy: a microspectroscopic comparison between femtosecond Ti: sapphire and Cr: forsterite laser sources. *Opt Quant Electron* 34:1251–1266
44. Mandal AK, Sreejith S, He T et al (2015) Three-photon-excited luminescence from unsymmetrical cyanostilbene aggregates: morphology tuning and targeted bioimaging. *ACS Nano* 9:4796–4805
45. Zhang Q, Wang X, Li PZ et al (2014) Biocompatible, uniform, and redispersible mesoporous silica nanoparticles for cancer-targeted drug delivery in vivo. *Adv Funct Mater* 24:2450–2461
46. Khajuria DK, Kumar VB, Karasik D et al (2017) Fluorescent nanoparticles with tissue dependent affinity for live zebrafish imaging. *ACS Appl Mater Interfaces* 9:18557–18565
47. Lee KJ, Nallathamby PD, Browning LM et al (2007) In vivo imaging of transport and biocompatibility of single silver nanoparticles in early development of zebrafish embryos. *ACS Nano* 1:133–143
48. Hill AJ, Teraoka H, Heideman W et al (2005) Zebrafish as a model vertebrate for investigating chemical toxicity. *Toxicol Sci* 86:6–19
49. Pyati UJ, Look AT, Hammerschmidt M (2007) Zebrafish as a powerful vertebrate model system for in vivo studies of cell death. *Semin Cancer Biol* 17:154–165

50. Wan Q, Song Y, Li Z et al (2013) In vivo monitoring of hydrogen sulfide using a cresyl violet-based ratiometric fluorescence probe. *Chem Commun* 49:502–504
51. Liu Y, Liu B, Feng D et al (2012) A progressive approach on zebrafish toward sensitive evaluation of nanoparticles' toxicity. *Integr Biol* 4:285–291
52. Wang Y, Seebald JL, Szeto KDP et al (2010) Biocompatibility and biodistribution of vivo and multiplex imaging. *ACS Nano* 4:4039–4053
53. Li K, Qin W, Ding D et al (2013) Photostable fluorescent organic dots with aggregation-induced emission (AIE dots) for noninvasive long-term cell tracing. *Sci Rep* 3:1150
54. Qian J, Zhu Z, Qin A et al (2015) High-order non-linear optical effects in organic luminogens with aggregation-induced emission. *Adv Mater* 27:2332–2339
55. Maiti M, Misra T, Bhattacharya T et al (2002) Comparative studies on inter-and intramolecular electron transfer processes within 4-methoxybenzo [b] thiophene (4MBT) and *p*-chloroacetophenone (PCA) reacting systems by using steady-state and laser flash photolysis techniques. *J Photochem Photobio A Chem* 152:41–52
56. Hu R, Lager E, Aguilar-Aguilar A et al (2009) Twisted intramolecular charge transfer and aggregation-induced emission of BODIPY derivatives. *J Phys Chem C* 113:15845–15853
57. Li D, Zhao X, Qin W et al (2016) Toxicity assessment and long-term three-photon fluorescence imaging of bright aggregation-induced emission nanodots in zebrafish. *Nano Res* 9:1921–1933
58. Kimmel CB, Ballard WW, Kimmel SR et al (1995) Stages of embryonic development of the zebrafish. *Dev Dyn* 203:253–310
59. Zhu Z, Qian J, Zhao X et al (2015) Stable and size-tunable aggregation-induced emission nanoparticles encapsulated with nanographene oxide and applications in three-photon fluorescence bioimaging. *ACS Nano* 10:588–597
60. Hummers WS, Offeman RE (1958) Preparation of graphitic oxide. *J Am Chem Soc* 80:1339–1339
61. Liu Z, Robinson JT, Sun XM et al (2008) PEGylated nanographene oxide for delivery of water-insoluble cancer drugs. *J Am Chem Soc* 130:10876–10877
62. Qian J, Wang D, Cai F et al (2012) Observation of multiphoton-induced fluorescence from graphene oxide nanoparticles and applications in in vivo functional bioimaging. *Angew Chem Int Ed* 51:10570–10575
63. Zhang HQ, Alifu N, Jiang T et al (2017) Biocompatible aggregation-induced emission nanoparticles with red emission for in vivo three-photon brain vascular imaging. *J Mater Chem B* 5:2757–2762
64. Wang YL, Han X, Xi W et al (2017) Bright AIE nanoparticles with F127 encapsulation for deep-tissue three-photon intravital brain angiography. *Adv Healthc Mater* 6(21):1700685
65. Wang YL, Chen M, Alifu N et al (2017) Aggregation-induced emission luminogen with deep-red emission for through-skull three-photon fluorescence imaging of mouse. *ACS Nano* 11:10452–10461
66. Jiang T, Qu Y, Li B et al (2015) Tetraphenylethene end-capped [1,2,5] thiadiazolo [3,4-c] pyridine with aggregation-induced emission and large two-photon absorption cross-sections. *RSC Adv* 5:1500–1506
67. Shen XY, Wang YJ, Zhao E et al (2013) Effects of substitution with donor-acceptor groups on the properties of tetraphenylethene trimer: aggregation-induced emission, solvatochromism, and mechanochromism. *J Phys Chem C* 117:7334–7347
68. Yeh HC, Yeh SJ, Chen CT (2003) Readily synthesised arylamino fumaronitrile for non-doped red organic light-emitting diodes. *Chem Commun* (20):2632–2633
69. Tang S, Li W, Shen F et al (2012) Highly efficient deep-blue electroluminescence based on the triphenylamine-cored and peripheral blue emitters with segregative HOMO–LUMO characteristics. *J Mater Chem* 22:4401–4408
70. Han X, Bai Q, Yao L et al (2015) Highly efficient solid-state near-infrared emitting material based on triphenylamine and diphenylfumaronitrile with an EQE of 2.58% in nondoped organic light-emitting diode. *Adv Funct Mater* 25:7521–7529

71. Wang Y, Ta VD, Gao Y et al (2014) Stimulated emission and lasing from CdSe/CdS/ZnS core-multi-shell quantum dots by simultaneous three-photon absorption. *Adv Mater* 26:2954–2961
72. Diao S, Blackburn JL, Hong G et al (2015) Fluorescence imaging *in vivo* at wavelengths beyond 1500 nm. *Angew Chem* 127:14971–14975
73. Qin A, Lam JWY, Mahtab F et al (2009) Pyrazine luminogens with “free” and “locked” phenyl rings: understanding of restriction of intramolecular rotation as a cause for aggregation-induced emission. *Appl Phys Lett* 94:253308